J. Fluid Mech. (2008), *vol.* 598, *pp.* 335–360.
doi:10.1017/S0022112007000055 Printed in the United Kingdom

Direct numerical simulation of passive scalar transport in transverse jets

SUMAN MUPPIDI AND KRISHNAN MAHESH

Aerospace Engineering and Mechanics, University of Minnesota, Minneapolis, MN 55455, USA

(Received 12 December 2006 and in revised form 16 November 2007)

Direct numerical simulation is used to study passive scalar transport and mixing in a round turbulent jet, in a laminar crossflow. The ratio of the jet velocity to that of the crossflow is 5.7, the Schmidt number of the scalar is 1.49, and the jet-exit Reynolds number is 5000. The scalar field is used to compute entrainment of the crossflow fluid by the jet. It is shown that the bulk of this entrainment occurs on the downstream side of the jet. Also, the transverse jet entrains more fluid than a regular jet even when the jet has not yet bent into the crossflow. The transverse jet's enhanced entrainment is explained in terms of the pressure field around the jet. The acceleration imposed by the crossflow deforms the jet cross-section on the downstream side, which sets up a pressure gradient that drives downstream crossflow fluid toward the jet. The simulation results are used to comment on the applicability of the gradient–diffusion hypothesis to compute passive scalar mixing in this flow field. Computed values of the eddy diffusivity show significant scatter, and a pronounced anisotropy. The near field also exhibits counter gradient diffusion.

1. Introduction

A jet in crossflow, or transverse jet, is a flow field where a jet of fluid enters and interacts with a crossflowing fluid. Practical examples include fuel injectors, smokestacks, film cooling on turbine blades and dilution holes in gas turbine combustors. A comprehensive review of past work on this problem is provided by Margason (1993). Previous workers have studied both the velocity field (Kamotani & Greber 1972; Fearn & Weston 1974; Andreopoulos & Rodi 1985; Krothapalli, Lourence & Buchlin 1990; Fric & Roshko 1994; Kelso, Lim & Perry 1996) and the passive scalar field (Smith & Mungal 1998; Su & Mungal 2004; Shan & Dimotakis 2006). Attempts at modelling the flow field were made by Broadwell & Breidenthal (1984), Karagozian (1986), Hasselbrink & Mungal (2001) and Muppidi & Mahesh (2005). Numerical simulations have been used in recent studies of transverse jets. Reynolds-Averaged Navier–Stokes (RANS) simulations of this flow field show differences when compared to experimental results (Chochua *et al.* 2000; Acharya, Tyagi & Hoda 2001). Large-eddy simulations (Yuan, Street & Ferziger 1999; Schluter & Schonfeld 2000) perform better in comparison. Muppidi & Mahesh (2007) obtained good agreement on comparing mean velocity and turbulent intensities from the direct numerical simulation (DNS) of a turbulent jet in crossflow, with the experimental results of Su & Mungal (2004).

Most applications of transverse jets involve mixing. The transverse jet shows increased decay of the scalar along its length, as compared to a regular jet, implying more effective mixing. Smith & Mungal (1998) show that the scalar centreline decay is

faster in the near field than that in the far field. They conclude that in the near field, the enhanced mixing is not an effect of the counter-rotating vortex pair (CVP) itself, but rather the process of CVP formation. Su & Mungal (2004) use planar laser-induced fluoresence (PLIF) and particle image velocimetry (PIV) to obtain velocity and scalar field data simultaneously. Shan & Dimotakis (2006) find increased mixing with an increase in the Reynolds number. Reynolds-number dependence is not observed in measures such as the scalar trajectory and the maximum mean-concentration decay, but is seen in the probability density function (PDF) of the jet fluid concentration.

The objective of the present paper is to study passive scalar transport and mixing characteristics in a round turbulent transverse jet, using DNS. The simulations are performed at conditions corresponding to the experiment by Su & Mungal (2004). The contributions of this paper are (i) a detailed discussion of agreement/disagreement of simulation results with experimental data, (ii) a quantitative discussion of the entrainment features of a transverse jet, and an explanation in terms of the pressure field, and (iii) an evaluation of the eddy-diffusivity hypothesis used to model scalar mixing in the RANS methodology. This paper is organized as follows. The simulation details are presented in § 2 – the problem is described in § 2.1, and the numerical details are briefly mentioned in §§ 2.2 and 2.3. Section 3 contains results of the simulation. Some characteristic features of the scalar field are presented in § 3.1. Section 3.2 compares the scalar mean and variance profiles, and turbulent scalar fluxes, between the simulation and the experiment. The scalar field is used to examine how the jet entrains crossflow fluid in § 3.3, and § 3.4 relates the dominant entrainment mechanisms to the pressure field. Section 4 uses the results of the simulation to comment upon the gradient–diffusivity hypothesis.

2. Simulation details

A brief description of the problem, algorithm and numerical details are presented in this section. Detailed descriptions of the numerical details for this problem – computational domain, computational mesh, boundary conditions etc. are available in Muppidi & Mahesh (2007).

2.1. *Problem*

The jet issues perpendicularly from a round pipe into the crossflow (figure 1). The crossflow and the jet are in the x and y directions, respectively. The velocity ratio, used to characterize a jet in crossflow, is defined as $r = \overline{u}_j/u_\infty$, where $\overline{u}_j$ is the mean jet velocity and u_∞ is the free-stream crossflow velocity. Conditions of the simulation are similar to an experiment by Su & Mungal (2004). The velocity ratio is 5.7 and the Reynolds number of the flow ($Re = u_j d/\nu$) is 5000. The jet is fully turbulent and the crossflow is laminar (with a boundary-layer thickness $\delta_{80\%} = 1.32d$ at the location of the jet exit, in the absence of the jet). In the experiment, the jet fluid is seeded with acetone vapour. This gives a density ratio $\rho_j/\rho_\infty = 1.1$, and a Schmidt number $Sc = 1.49$. In the present simulations, the densities of the jet and crossflow fluids are taken to be the same, and the passive scalar Schmidt number is the same as that in the experiment.

2.2. *Algorithm*

The algorithm solves the incompressible Navier–Stokes equations,

$$\frac{\partial u_i}{\partial t} + \frac{\partial u_i u_j}{\partial x_j} = -\frac{\partial p}{\partial x_i} + \nu \frac{\partial^2 u_i}{\partial x_j x_j}, \frac{\partial u_i}{\partial x_i} = 0, \tag{2.1}$$

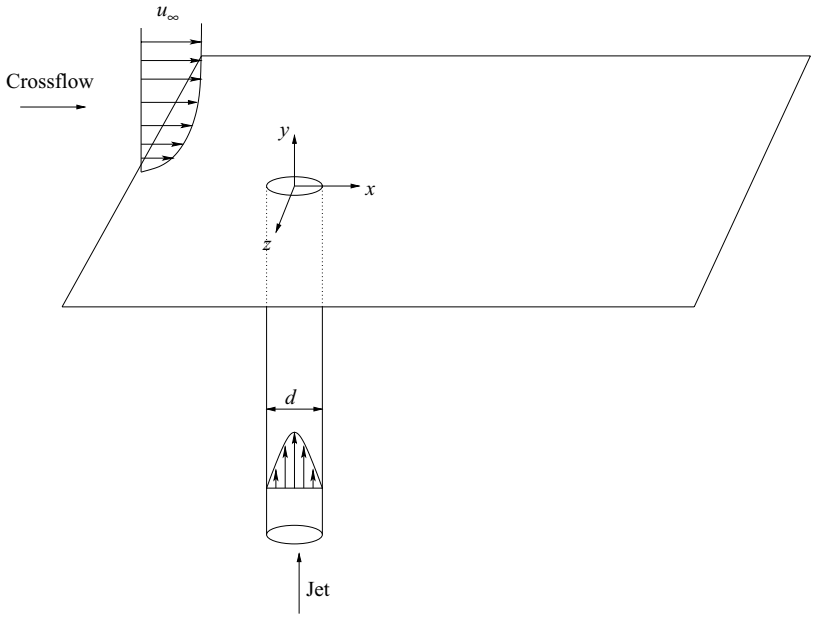

FIGURE 1. Schematic of the problem.

on unstructured grids. u_i, p and ν denote the velocities, pressure and kinematic viscosity, respectively. The numerical scheme is described in detail in Mahesh, Constantinescu & Moin (2004). The algorithm is a predictor–corrector formulation and emphasizes discrete energy conservation on unstructured grids. This property makes the computations robust at high Reynolds numbers without numerical dissipation. The velocity and pressure fields are stored at the control volume centroids, and are integrated in time implicitly using a Crank–Nicolson scheme.

The passive scalar is computed by solving the advection–diffusion equation

$$\frac{\partial C}{\partial t} + \frac{\partial C u_j}{\partial x_j} = \frac{\nu}{Sc} \frac{\partial^2 C}{\partial x_j x_j}, \tag{2.2}$$

where C is the concentration of the scalar, and is stored at the control volume centroids. The jet fluid has a value of $C = 1.0$, and the crossflow fluid has $C = 0$. Equation (2.2) is different from (2.1) because of the absence of the pressure term. The advection term can generate sharp gradients by transporting high momentum/scalar fluid into a region of low momentum/scalar. However, the pressure gradient term and the divergence-free condition have a 'smoothing' effect on the momentum field. The scalar field has no such mechanism, and scalar gradients tend to be higher than velocity gradients even when the Schmidt number is 1. This behaviour affects the algorithm/solution in two ways. Sharp gradients yield high frequencies and, as a result, the stable computational time-step required to advance the scalar is significantly smaller than that for the velocity field. Also, sharp gradients give rise to dispersive errors, which affect the boundedness of the scalar. The algorithm must address these features without compromising the overall efficiency.

The present simulations are performed by using different time-steps for the scalar and the velocity fields. The velocity field is advanced implicitly using a Crank–Nicolson scheme (time step Δt_v), and the passive scalar field is advanced in an inner

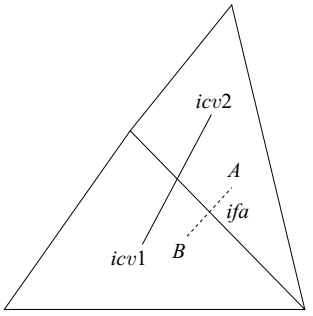

FIGURE 2. Schematic of the reconstruction.

loop using a fourth-order Runge–Kutta scheme (time step Δt_s). The ratio $\Delta t_v/\Delta t_s$ is around 20 for the present simulations. As compared to using the same time-step (Δt_s) for advancing both the scalar and velocity fields, this approach results in significant savings in the wall-time required for the simulation.

To avoid dispersive errors (and resulting overshoot for the values of passive scalar concentration), the scalar transport is computed using a predictor-corrector method. First, the scalar field is advanced using a second-order central difference scheme. This predicted scalar field is corrected in regions of scalar overshoot using a first-order upwind scheme. The corrector step ensures that locally, the passive scalar concentration is bounded (i.e. $C \in [0,1]$), and is based on the work by Herrmann, Blanquart & Raman (2004).

Finally, the scalar fluxes are computed using a reconstruction scheme based on least-squares. Equation (2.2) requires the values of the scalar (C_f, for the convective term) and the face–normal gradient ($\mathrm{d}C_f/\mathrm{d}N$, for the viscous term) at the centroid of the control volume faces (see Mahesh *et al.* 2004 for details). For each face, these values must be interpolated using the values of the scalar at the centroids of the neighbouring control volumes. Consider the control volumes $icv1$ and $icv2$ shown in figure 2. The common face is ifa. The easiest interpolation is to use

$$C_{ifa} = 0.5(C_{icv1} + C_{icv2}), \qquad \frac{\mathrm{d}}{\mathrm{d}N} C_{ifa} = \frac{C_{icv2} - C_{icv1}}{d_{ifa}} \ . \tag{2.3}$$

(By convention, the direction of the face normal is from *icv1* to *icv2*.)

Here, d_{ifa} is the distance between the centroids of $icv1$ and $icv2$. Although this approximation provides good results on uniform/structured grids, (2.3) results in significant errors on a control volume such as the one shown in figure 2. The face centroid might not be equidistant from the centroids of *icv1* and *icv2*, and the line joining the cell centroids neither passes through the face centroid, nor is normal to the face. The new reconstruction scheme identifies two points A and B (figure 2) that are on either side of the face *ifa*, equidistant from the face centre, and such that the line A–B both passes through the face centre and is normal to the face. It is easy to see that if the scalar concentration at A and B are known, the interpolations

$$C_{ifa} = 0.5(C_A + C_B), \qquad \frac{\mathrm{d}}{\mathrm{d}N} C_{ifa} = \frac{C_A - C_B}{d_{AB}} \tag{2.4}$$

provide a more accurate measure of the flux than do those in (2.3). Since the value of the scalar at the cell centroids is known, the gradient $\partial C/\partial x_i$ at the cell centres can be computed using a least-squares approach as follows.

Consider a hexahedral control volume (*icv*) with six neighbouring cells (*icv1* to *icv6*), the values of the scalar at whose centres are known. The scalar values at the

neighbouring cells can be written as

$$C_{icv1} = C_{icv} + \{\nabla C_{icv}\} \cdot \{\Delta \boldsymbol{x}_{icv1-icv}\} \text{ etc.} \tag{2.5}$$

Since C_{icv1} to C_{icv6} are known, an error term can be defined as

$$\epsilon_1 = C_{icv1} - C_{icv} - \nabla C_{icv} \cdot \Delta x_{icv2-icv} \text{ etc.} \tag{2.6}$$

Minimizing $E = {\epsilon_1}^2 + {\epsilon_2}^2 + \cdots + {\epsilon_6}^2$ yields ∇C_{icv} using the least-squares approach.

Next, C_A and C_B are obtained using

$$C_A = C_{icv2} + \left(\frac{\partial C}{\partial x_j}\right)_{icv2} (x_{j,A} - x_{j,icv2}) \text{ etc.}, \tag{2.7}$$

and (2.4) is used to compute the fluxes. This interpolation yields reasonable solutions even on meshes with high aspect ratio and/or high skewness.

2.3. *Computational domain and boundary conditions*

The computational domain extends $32d \times 64d \times 64d$ in the axial, wall-normal and spanwise directions (x, y and z), respectively, and includes a $2d$ length of the pipe. The crossflow inflow plane is located $4d$ upstream of the jet exit. Preliminary computations showed that a domain of this size does not constrain the jet, and the flow does not feel the effects of confinement by the boundary, thus allowing the interaction between the jet and crossflow fluids to occur naturally.

The crossflow is modelled as a laminar flow past a flat plate (Schlichting 1968). Based on the analytical solution to the Blasius boundary layer, a velocity field is specified at the inflow plane of the crossflow such that in the absence of the jet, the crossflow has the prescribed $\delta_{80\%}$ at the centre of the jet exit. In order to simulate a fully turbulent jet, a separate simulation of fully developed turbulent flow in a pipe is performed. The Reynolds number for this computation, based on the pipe diameter and the mean axial velocity, is 5000. The velocity field at a cross-section (normal to the pipe axis) from this simulation is stored over a length of time, and input at the inflow plane of the pipe ($y = -2d$) as the time-dependent boundary condition for the jet in the present simulation. The crossflow boundary condition is validated by comparing velocities with the similarity solution and the jet boundary condition is validated by comparing mean velocities and turbulent intensities with the existing results of Eggels *et al.* (1994). Both validations are shown in Muppidi & Mahesh (2007). On the exit plane ($x/d = 32$), a zero-gradient boundary condition is used for the velocities. On the spanwise boundaries ($z/d = \pm 32$), the velocity field corresponding to the laminar crossflow is specified. Free-stream velocity boundary conditions are specified on the top boundary ($y/d = 64$).

At the pipe inflow ($y = -2d$), a scalar concentration of $C = 1.0$ is enforced, so that the jet fluid carries the passive scalar. The crossflow inflow plane is specified as $C = 0$. A zero-gradient boundary condition for the scalar is enforced at the walls, spanwise boundaries, top boundary and the outflow boundary. The computational mesh is unstructured and consists of approximately 11 million hexahedral elements.

3. Results

The velocity field was compared with profiles of the mean jet trajectory, mean velocity and turbulent intensities available from the experiment, and good agreement was obtained (Muppidi & Mahesh 2007).

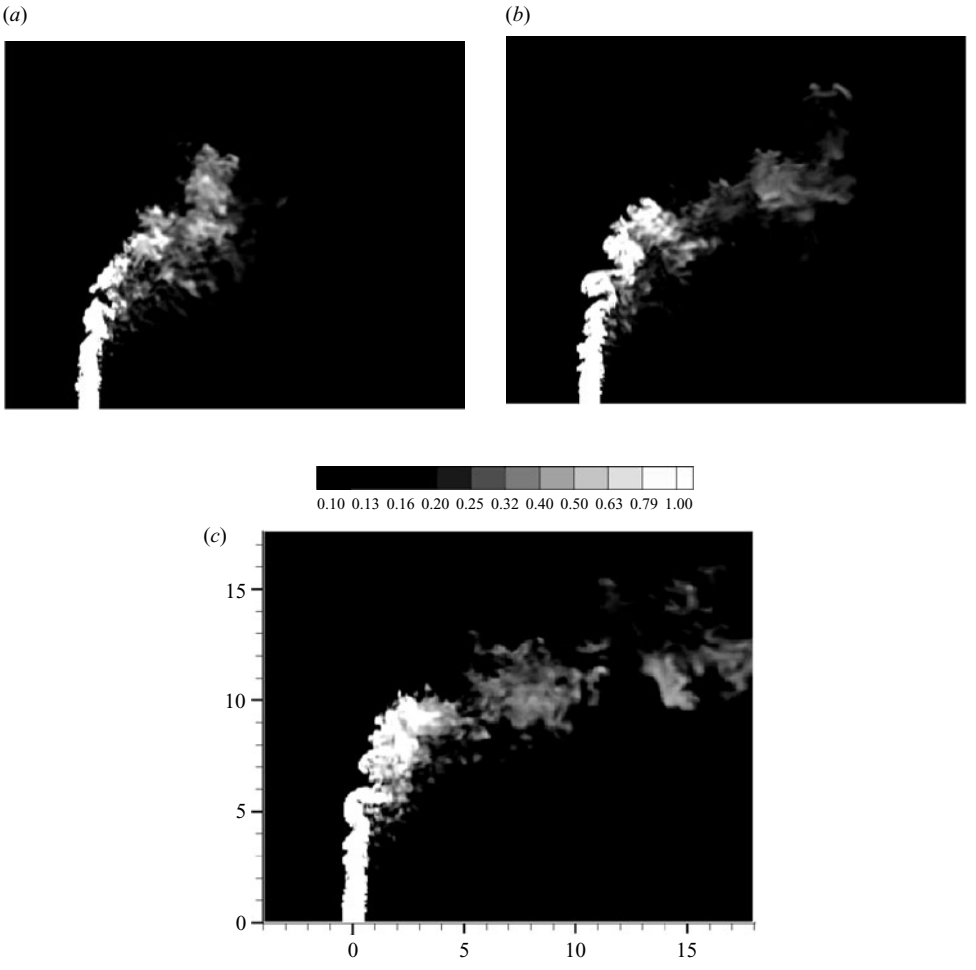

FIGURE 3. Instantaneous contours of passive scalar on the symmetry plane at different time instants after the scalar has been introduced into the flow.

3.1. *Scalar field*

Figure 3 shows the instantaneous contours of passive scalar concentration on the symmetry plane. Note that the scalar is introduced into the flow only after the velocity field is considered to be statistically stationary, i.e. after the transients exit the flow domain. Hence, these figures represent the physical solution, and not a numerical transient. The Kelvin–Helmholtz instability mechanism gives rise to rollers on the windward side of the jet. The characteristic length of these rollers appears to increase along the jet length, as long as the jet is almost vertical. The largest rollers are observed where the jet begins to bend into the crossflow, about 5–8 d past the jet exit.

On the downstream side of the jet, figure 3 shows 'fingers' or 'filaments' of jet fluid reaching into the crossflow fluid, normal to the jet trajectory. Figure 3(c) is similar to figure 4(a) of Su & Mungal (2004), who make the same observation. Su & Mungal suggest these scalar filaments probably correspond to the wake vortices. Fric & Roshko (1994) explain the formation of the wake vortices as a result of the separation events in the crossflow boundary layer (below the jet, as it bends). They also show that the wake vortices are observed only when the crossflow fluid is

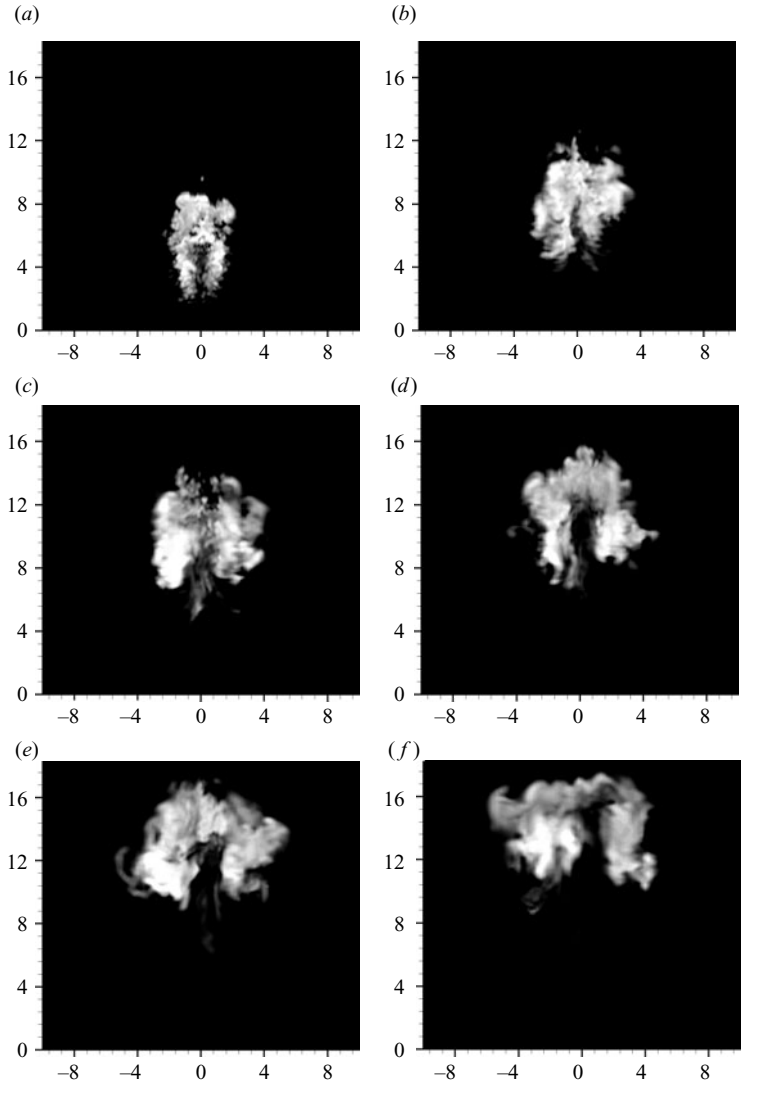

FIGURE 4. End views show instantaneous contours of passive scalar. (*a*) $x = d$, (*b*) $x = 4d$, (*c*) $x = 7d$, (*d*) $x = 10d$, (*e*) $x = 15d$ and (*f*) $x = 20d$. All the figures correspond to the same instant of time.

seeded, and not when the jet fluid is seeded, signifying that the crossflow boundary-layer vorticity contributes to the vorticity in the wake vortices. It is the jet fluid that is seeded in the present simulation and in the experiments of Su & Mungal (2004) and Smith & Mungal (1998). The experiments of Smith & Mungal show that the presence of jet fluid in its wake becomes more noticeable as the velocity ratio increases from $r = 5$ to 10 to 20 (figures 11*b*, 12 and 15, respectively, of their paper). By extending the Fric & Roshko mechanism, Smith & Mungal propose that the axial flow through the wake vortices causes the presence of jet fluid in the wake region. Shan & Dimotakis (2006) observe these filaments in their experiments at $r = 10$ and $r = 32$. Figure 4 shows the end views of instantaneous passive scalar concentration at different downstream locations. Note that all the snapshots correspond to the same instant in time. Figure 4, along with figure 3, shows that the jet fluid filaments are

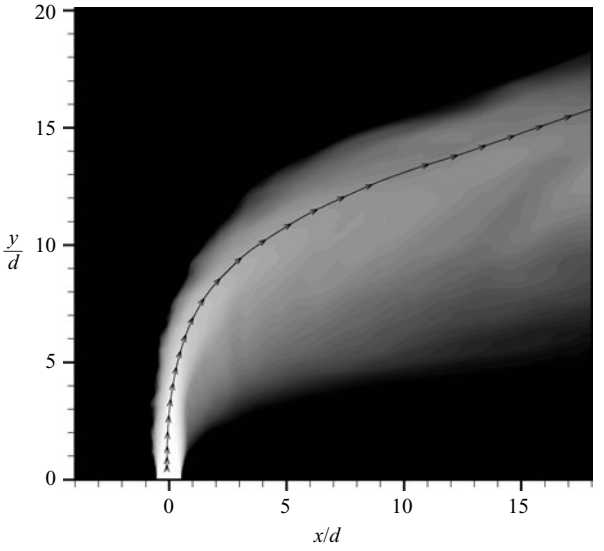

FIGURE 5. Time-averaged contours of passive scalar concentration on the symmetry plane. Also shown is the mean centre streamline, indicating the jet trajectory.

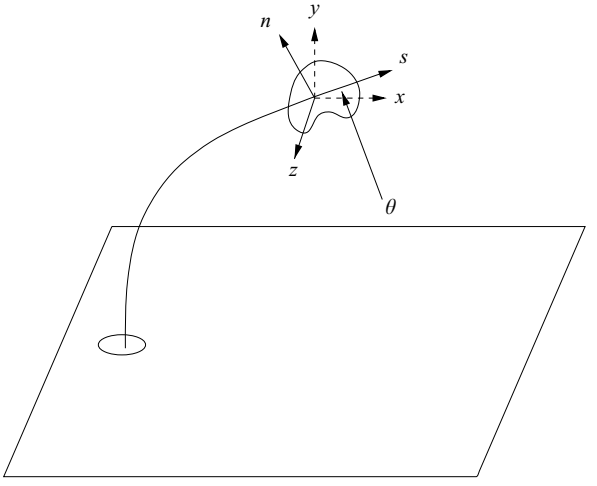

FIGURE 6. Schematic of the coordinate system that is aligned with the jet trajectory.

observed on the symmetry plane, exist very close to it, and are virtually non-existent on off-symmetry planes.

Contours of time-averaged scalar concentration on the symmetry plane are shown in figure 5. The centre streamline, which denotes the mean jet trajectory, is also shown. Figure 5 shows that the mean scalar concentration decreases with increasing distance from the jet exit. Also, the jet width is larger on the downstream side than on the upstream side of the centre streamline. This asymmetry is also observed in contours of mean velocity magnitude on the symmetry plane, and has been noted by Su & Mungal (2004). Qualitatively, figures 3 and 5 are similar to those available from the experiment.

The jet width can be quantitatively studied by plotting the scalar concentration in a trajectory based coordinate system (figure 6). Here, s is the distance from the jet

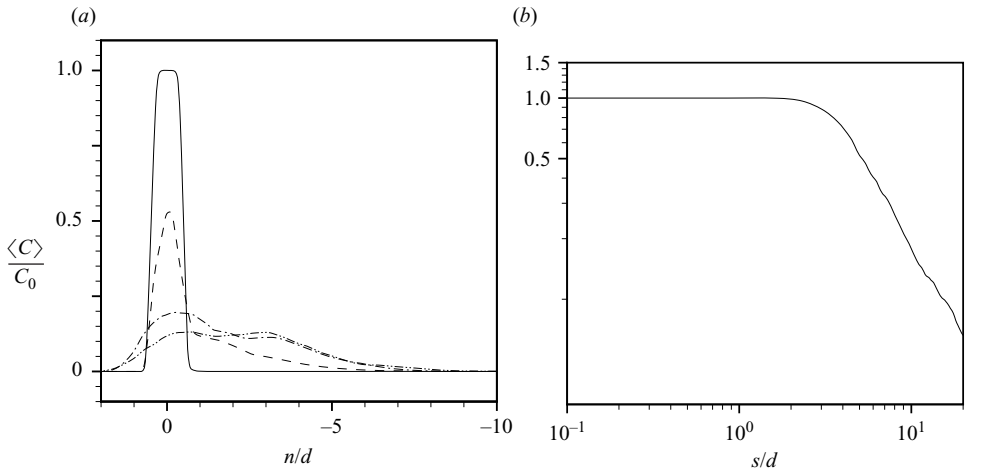

FIGURE 7. (*a*) Variation of mean scalar concentration along the trajectory-normal variable n. The profiles correspond to $s = d$ (———), $5d$ (– – –), $10d$ (—·—), and $15d$ (—··—). (*b*) Scalar decay along the mean jet trajectory.

exit, along the centre streamline, and n is the coordinate normal to the trajectory. The (s, n)-plane is the same as the (x, y)-plane, and the z coordinate is the same in both the coordinate systems. Figure 7(*a*) shows the variation of the mean scalar concentration with n. The curves correspond to different downstream distances. At any s, $n = 0$ corresponds to the centre streamline.

At the location $s = d$, the peak scalar concentration is C_0 across almost the entire jet edge. Past the jet edge, both downstream and upstream, the fluid contains no scalar, and the gradients near the jet edge are sharp. At the next location, $s = 3d$, the peak scalar concentration is lower than C_0 and occurs at $n = 0$. On the upstream side, there is no scalar past the leading edge of the jet. However, on the downstream side, a small amount of scalar is observed up to a distance of about $2.5d$ past the jet centreline. As a result, if the jet width were based on a cutoff scalar concentration ($C/C_0 = 0.1$, say), the jet width downstream of the centre streamline is greater than that upstream. This trend continues along the jet trajectory: peak C decreases and the jet width on the downstream side increases. By $s = 10d$, the peak scalar concentration values are comparable to the scalar concentration across the jet width, resulting in a nearly uniform profile. Consistent with the observations of Smith & Mungal (1998), the present results show that the decrease in peak scalar concentration is greater between $s = 5d$ and $10d$ as compared to that between $10d$ and $15d$. Figure 7(*a*) indicates that the scalar concentration goes to zero at about the same value of n/d at both $s = 10d$ and $s = 15d$. Su & Mungal show similar behaviour in figure 12 of their paper. Their profiles at $s = 2$, 3 and $4rd$ appear to go to zero around the same points: $n = 0.25rd$ and $-1.2rd$. Note that figure 7(*a*) shows only the behaviour of the scalar profiles on the symmetry plane. In contrast to this behaviour, the volume flux (figure 14*a*) and the cross-section area (figure 15*b*) of the scalar carrying fluid increase monotonically with s. Figure 7(*b*) shows the passive scalar decay along the jet trajectory. The mean scalar concentration remains constant up to about $s = 2d$ and decays thereafter.

3.2. *Comparison to experiment*

Scalar data from the simulation is compared to that from the experiment of Su & Mungal (2004). Figure 8(*a*) shows the comparison of mean scalar, while figure 8(*b*)

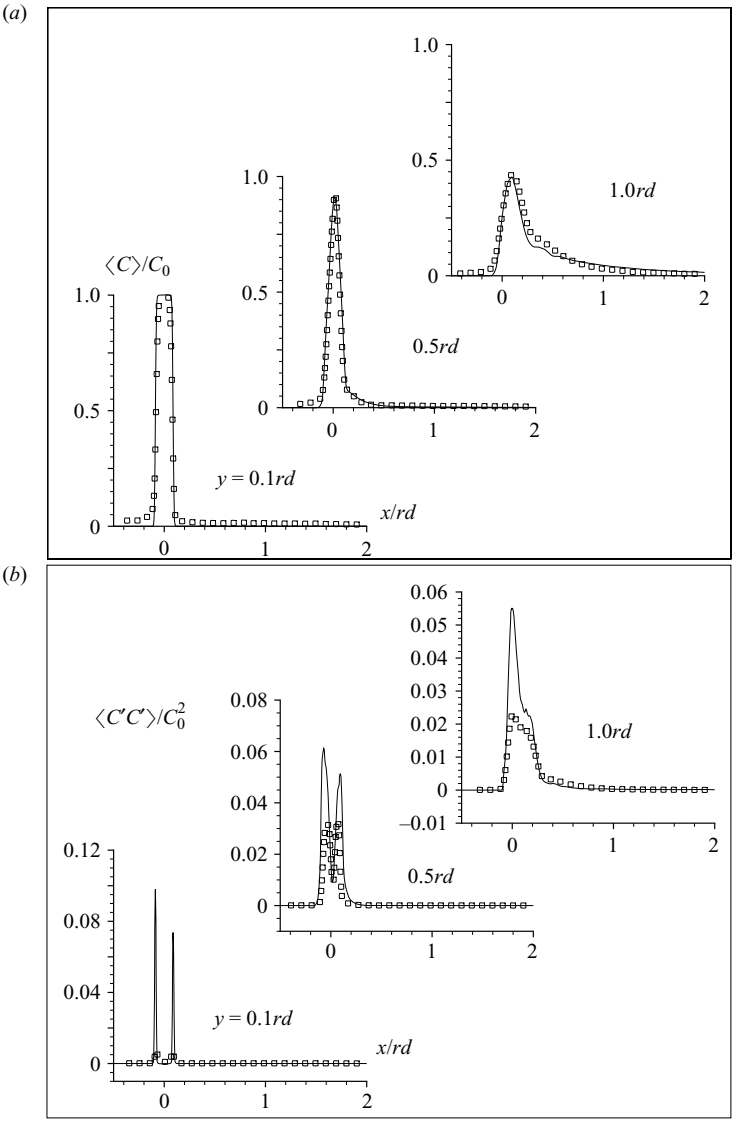

FIGURE 8. Comparison of mean and variance profiles of the passive scalar on the symmetry plane. ———, simulation; □, Su & Mungal's experiment.

shows that of the scalar variance $\langle C'C' \rangle$. The lines are the profiles from the simulation and the symbols show the experimental profiles. The profiles correspond to the symmetry plane, and to three vertical locations: $y = 0.1rd$, $0.5rd$ and $1.0rd$. Both $\langle C \rangle$ and $\langle C'C' \rangle$ are normalized with the mean scalar concentration at the jet exit C_0. Figure 8(a) shows that close to the wall, the mean scalar profile is symmetric (about the centre of the jet exit) and is characterized by sharp gradients corresponding to the jet edges. With increasing distance from the wall, the gradients become less sharp, and the profiles lose the symmetry. As the jet fluid mixes with the crossflow fluid, peak scalar concentration decreases from $y/rd = 0.1$ to 0.5 to 1.0. At the farthest station, note that the peak $\langle C \rangle$ is about half of that at the jet exit.

Profiles of the scalar variance (figure 8*b*) exhibit two peaks at $y/rd = 0.1$, corresponding to the leading and trailing edges of the jet. Moving away from the wall, the value of the peak decreases, and by the farthest station, the profile shows a single peak. It appears that the shear layers, corresponding to the edges of the jet, collapse between $y/rd = 0.5$ and $y/rd = 1.0$. In this regard, the $\langle C'C' \rangle$ profiles are similar to that of $\langle u'u' \rangle$ and $\langle v'v' \rangle$ (Muppidi & Mahesh 2007). Also, peak $\langle C'C' \rangle$ decreases with increasing distance from the jet exit.

Comparison of the mean scalar profiles shows good agreement between the simulation and the experiment. This is true even at the station closest to the wall ($y/rd = 0.1$), where the profile is characterized by steep gradients. In contrast, the profiles of mean scalar variance $\langle C'C' \rangle$ show some disagreement. At $y = 0.1rd$, the peak intensity from the simulation is almost ten times that from the experiment. At the other two locations, the peak magnitudes vary by a factor of about two. Note that the velocity field comparisons were made at the same three locations (Muppidi & Mahesh 2007). Profiles of mean velocity $\langle v \rangle$ and turbulent intensities $\langle u'u' \rangle$, $\langle v'v' \rangle$ and $\langle u'v' \rangle$ show good agreement with experimental results (figures 6 and 7 of that paper).

Details of the simulation and numerics were re-inspected in order to clarify the source of this disagreement. Some of the numerics were even modified to ensure that the observed higher values of peak $\langle C'C' \rangle$ were not algorithm-induced. The rest of this section provides a few details of this process. Considerable care was taken to match the conditions of the simulation to that of the experiment. The Reynolds number and the velocity ratio of the flow in the simulation are the same as that of the experiment (5000 and 5.7, respectively). The boundary condition for the crossflow is specified so that the crossflow boundary-layer thickness at the location of the jet exit (in the absence of the jet) matches that in the experiment ($\delta_{80\%} = 1.32d$) exactly. The Schmidt number for the passive scalar is also matched ($Sc = 1.49$).

It was ensured that the transients (both velocity and scalar fields) exit the flow domain before computing the statistics. The passive scalar was introduced into the flow domain only after the velocity field is statistically stationary and devoid of any transients. The velocity field profiles converge after about 30 units (d/u_∞) of time. This was observed by comparing statistics computed over about 120 units of time. The mean scalar profiles converge and show good agreement after about 25–30 units of time. The mean scalar variance profiles presented here were plotted after compiling statistics over 60 units of time. Note that between 30 and 60 units of time, the level of difference (between the simulation and the experiment) does not change.

In order to rule out the numerical technique as the source of the observed disagreement (between the simulation and the experiment), the simulation was performed using a few variations of the numerics. Each of these simulations was initialized with a statistically stationary velocity field with no fluid containing any passive scalar ($C = 0$ everywhere in the domain). The solution was advanced until the scalar transients exit the domain, and statistics were then computed over about 60 units of time. The choices for the passive scalar algorithm were: first-order spatial interpolation (equation (2.3)) *vs.* second-order interpolation (equation (2.4)), constant scalar upwind parameter *vs.* predictor–corrector scheme (section (2.2)) to compute the fluxes, and second-order Adams–Bashforth *vs.* fourth-order Runge–Kutta scheme to advance the scalar in time.

In the first implementation, the computation used a constant upwind parameter, first-order spatial discretization, and an Adams–Bashforth scheme to advance in time. Next, the spatial discretization was changed to the second-order scheme. This did not decrease the difference. The predictor–corrector approach was implemented to

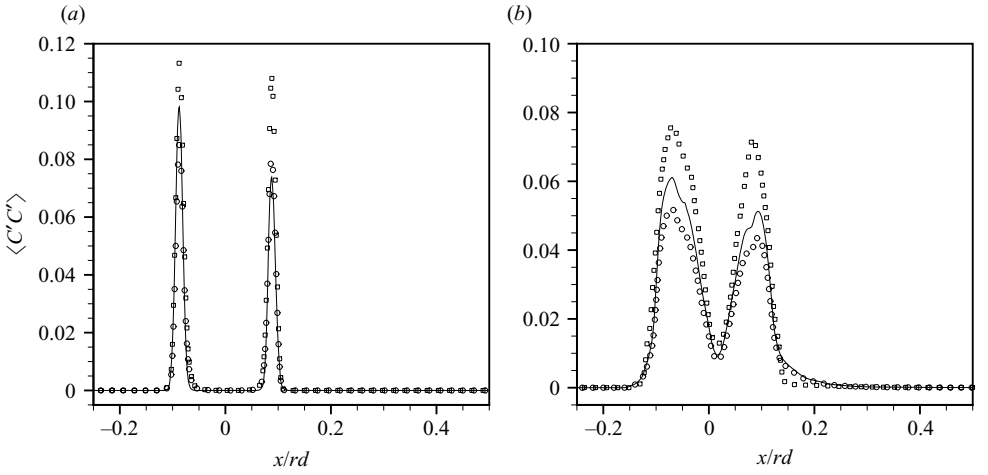

FIGURE 9. Profiles of scalar variance at (*a*) $y/rd = 0.1$ and (*b*) $y/rd = 0.5$ using no upwinding (□, $\omega = 0$), upwinding (○, $\omega = 0.3$) and the predictor–corrector approach (———). Note that even a fully dissipative scheme results in peak $C'C'$ values that are much higher than that from the experiment.

compute the scalar, and the fourth-order Runge–Kutta scheme was used to advance in time. Results from all these simulations show a similar level of deviation, comparable to that in figure 8, from the experiment.

Figure 9 shows the profiles of $\langle C'C' \rangle$ at two stations from three different simulations. The solid lines represent the results using the predictor–corrector approach (and correspond to the profiles in figure 8). The square symbols are results obtained using no upwinding (second-order central difference). The circles indicate the results obtained with upwinding ($\omega = 0.3$). As expected, the peak scalar variance decreases when ω is changed from 0 to 0.3, and this decrease is about 30%. Also, the peak variance using the predictor–corrector scheme is in between the squares and the circles. The behaviour of the different schemes was studied by computing a periodic one-dimensional advection–diffusion problem with a square wave initial condition. It was observed that the profile with $\omega = 0$ was extremely dispersive while the profile with $\omega = 0.25$ showed significant dissipation. The predictor–corrector approach provides the best solution, with neither dispersive errors nor large dissipation of gradients. Based on the results of the test problem, we believe the predictor–corrector scheme to provide the best possible solution. Finally, figure 9 shows that although an increase in ω decreases the peak $\langle C'C' \rangle$, the lower peaks are still significantly higher than the peak variance values obtained from the experiment.

It must be noted, from figure 8(*b*) that even when the profiles show huge differences in peak $\langle C'C' \rangle$ ($y/rd = 0.1$, 0.5), reasonable agreement is observed on the centreline. The spatial evolution of a round turbulent jet was performed using the same base scheme at a Reynolds number of 2400 (Babu & Mahesh 2004). Results from that simulation, when compared to existing experimental data, show a reasonable agreement for the scalar r.m.s., both on the centreline and in the vicinity of the jet shear layer. Figure 10 plots the variation of $\langle C'C' \rangle$ with the similarity variable $\eta = r/(z - z_0)$ where r and z are the radial and axial coordinates, respectively, and z_0 is the location where the potential core closes. The figure shows scalar r.m.s. profiles obtained from two simulations on two different computational meshes. The 50 million

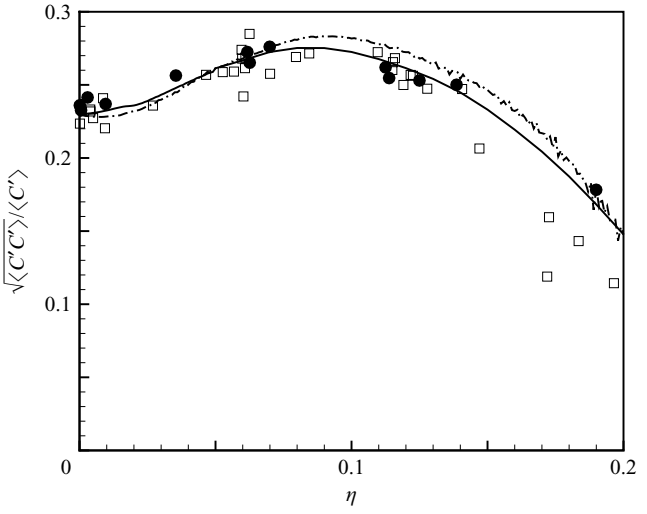

FIGURE 10. Scalar transport in a round turbulent jet. Profile of scalar variance plotted against the similarity variable, the results are from Babu & Mahesh (2004). ——, DNS, 50 million grid; —·—, DNS, 6 million grid; □, Dowling & Dimotakis (1990, $Re = 5000$); •, Dowling & Dimotakis (1990, $Re = 16\,000$).

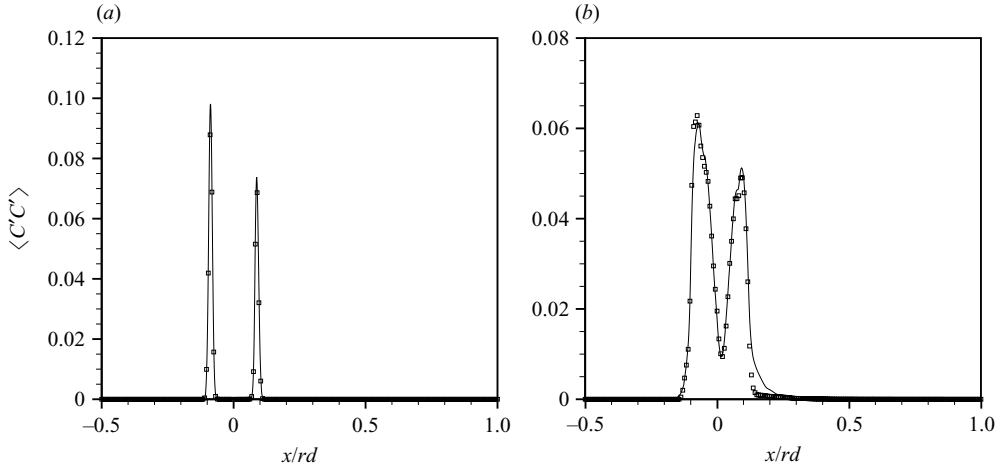

FIGURE 11. Profiles of the scalar variance at (*a*) $y/rd = 0.1$ and (*b*) $y/rd = 0.5$. The symbols show profiles obtained after filtering the solution to a resolution (in the x and y directions) similar to the experiment.

mesh has over twice the resolution (in the x, y and z directions) in the vicinity of the jet, as compared to the 6 million mesh.

The experiment averages the scalar field over a rectangular box (in the (x, y)-plane), affecting the final resolution. Similar averaging is present in the third dimension over the thickness of the laser sheet. It is therefore possible that the experiment might underpredict the scalar variance while finding the mean scalar accurately. The measurement window in the experiments is about $3.5rd \times 3.5rd$ (in the x and y directions), and the experiments provide a 512×512 pixel image. This translates to a resolution of $\Delta x = \Delta y = 0.038d$, which is of the same order as the computational mesh used for the simulation. Figure 11 shows profiles of the scalar variance at

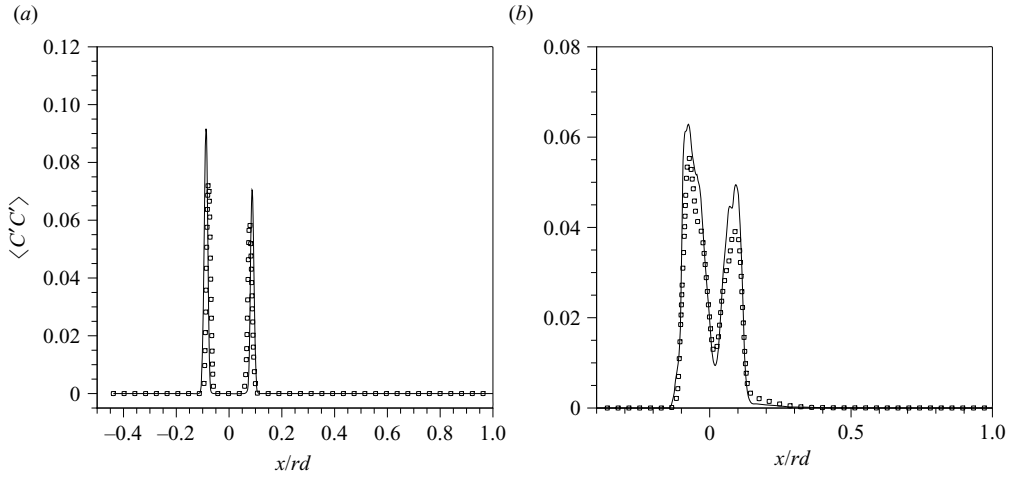

FIGURE 12. Profiles of the scalar variance at (*a*) $y/rd = 0.1$ and (*b*) $y/rd = 0.5$. The symbols show profiles belonging to the off-symmetry plane $z/d = 0.1105$.

$y/rd = 0.1$ and $y/rd = 0.5$, from the simulation. The solid lines are the same as that shown in figure 8. The solution on the symmetry plane (over a $3.5rd \times 3.5rd$ region corresponding to the measurement window in the experiment) is interpolated onto a regular mesh containing 512 points in the x and y directions. The resulting profiles are shown in figure 11 using symbols. Note that the peak variance does not decrease significantly.

In the spanwise direction, the thickness of the laser sheet (used in the experiment for visualization) varies between 500 and 1000 μm. This translates to a resolution of $\Delta z \sim 0.1105d - 0.221d$, larger than the mesh elements used in the simulation. Significantly, the experimental Δz is comparable to the jet exit diameter. Figure 12 shows profiles of $\langle C'C' \rangle$ along the streamwise distance, on the symmetry plane, and on the off-symmetry plane $z/d = 0.1105$, the location corresponding to the maximum laser-sheet thickness. We observe that the peak variance is slightly lower on the off-symmetry plane than on the symmetry plane, and also that the distance between the peaks is smaller. While a filtered result (filtered in the z direction, over a distance corresponding to the laser-sheet thickness) would result in a lower peak scalar variance, it does not appear that the decrease will be large enough for the filtered profile to agree with the experimental profile. At this point, the reasons for the poor agreement of $\langle C'C' \rangle$ are unknown.

Figure 13 shows the turbulent scalar fluxes $\langle u'C' \rangle$ and $\langle v'C' \rangle$ at the same three locations (as figure 8) on the symmetry plane. Like turbulent intensities and $\langle C'C' \rangle$, profiles of the fluxes are characterized by steep gradients at $y/rd = 0.1$, which grow less steep away from the wall. Note that that peak $\langle u'C' \rangle$ does not differ much between the three locations. The comparisons show, similar to figure 8(*b*), that the peak fluxes obtained from the simulation are higher than that from the experiment. This disparity is highest at $y/rd = 0.1$. The best agreement is observed in the profile of $\langle u'C' \rangle$ at $y/rd = 0.5$.

3.3. *Entrainment*

Entrainment of the crossflow fluid by the jet is computed using the volume flux of the scalar-carrying fluid across the trajectory-normal planes. Figure 14(*a*) shows the volume flux (normalized by its value at the jet exit) as a function of the distance from

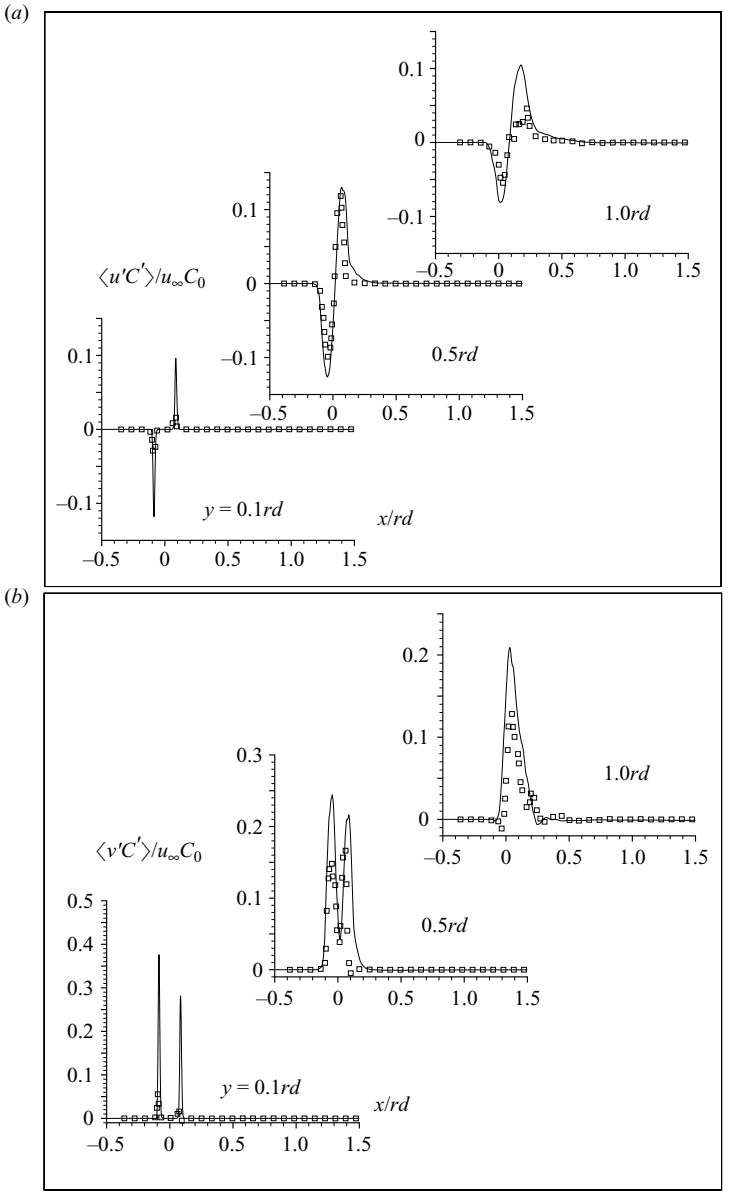

FIGURE 13. Comparison of profiles of turbulent scalar fluxes ($\langle u'C'\rangle$ and $\langle v'C'\rangle$) on the symmetry plane. ———, simulation; □, Su & Mungal's experiment.

the jet exit. The figure also shows the Ricou–Spalding correlation (Ricou & Spalding 1961) for the volume flux in a regular jet, where entrainment increases linearly with distance from the jet exit. Note that entrainment in the transverse jet is significantly larger than that in a regular jet. A similar result has been shown by Yuan & Street (1998). Note that their results (figures 11 and 12 of their paper) correspond to the flow field after the jet bends into the crossflow ($s \sim 4d$). Figure 14(a) shows that entrainment in the transverse jet is about twice that in the regular jet at a distance of $6d$; and at a distance of $9d$, the entrainment is about three times as much. At the jet exit, $s = 0$ and $V_s = V_0$, for both the regular jet and the transverse jet. At a distance d,

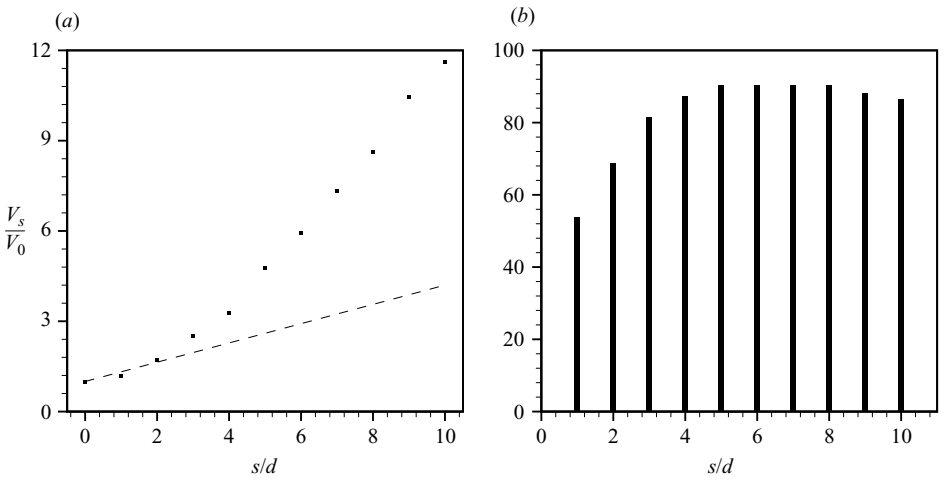

FIGURE 14. (*a*) Volume flux of the scalar carrying fluid plotted along the length of the jet. – – –, Ricou–Spalding correlation for entrainment in a regular jet. (*b*) Percentage contribution of the downstream side of the jet, to the total entrainment, plotted as a function of the jet length.

the regular jet's entrainment is greater than that of the jet in crossflow. At a distance of 2 diameters downstream, the entrainment appears the same for both. Thereafter, figure 14(*a*) shows an acute increase in the entrainment in a transverse jet. Note that these values reflect this flow field at $r = 5.7$. It is conceivable that a transverse jet of a different velocity ratio would show quantitatively different entrainment characteristics.

The solution is used to compute entrainment on the upstream and downstream sides of the jet separately. Figure 14(*b*) shows the percentage contribution of the downstream side of the jet to the total entrainment. Close to the jet exit, both the downstream and upstream sides of the jet contribute about the same to the total entrainment, and in this region, the transverse jet's entrainment is roughly the same as that of a regular jet, as observed in figure 14(*a*). Moving further, the contribution of the downstream side increases significantly. For example, at a distance of $6d$ from the jet exit, the upstream side contributes to only about 10% of the total entrainment. It appears that the increased entrainment (of the transverse jet as compared to the regular jet) past $2d$ roughly corresponds to the increased contribution of the downstream side of the jet to the total entrainment, as opposed to the mechanism proposed by Yuan & Street (1998) that suggests entrainment on the upstream face increases as the jet bends into the crossflow.

Figure 15(*a*) shows the time-averaged streamlines on the symmetry plane. Streamlines emanating from the leading and trailing edges of the jet exit indicate the jet boundary. Other streamlines indicate the motion of the crossflow fluid. Streamlines entering the domain from the crossflow boundary, upstream of the jet, bend in the direction of the jet fluid – and appear to almost merge with the leading-edge boundary of the jet. These streamlines must account for the upstream side entrainment of the jet. In addition, the jet entrains fluid on the downstream side, as seen from the streamlines downstream of the jet's trailing edge, and the source of this entrainment is the node (observed near $x \sim 2.5d$, $y \sim 1.8d$), whose presence is well documented (e.g. Kelso *et al.* 1996). The local flow field acts as a source in the symmetry plane (note the streamlines fanning out across the plane) and as a sink in the horizontal

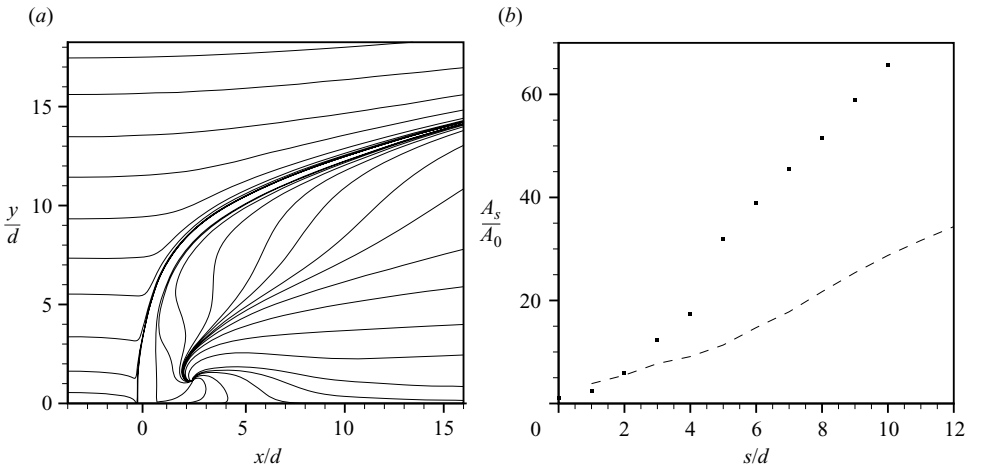

FIGURE 15. (*a*) Mean streamlines on the symmetry plane. (*b*) Jet area variation along jet length. – – –, the same for a regular turbulent jet (Babu & Mahesh 2004).

plane (the streamlines pass around the jet and converge toward this node). Owing to this dual behaviour, this point is sometimes termed the 'saddle-node'. The intensity of the downstream entrainment is high, as seen from the steep angle of the streamlines toward the jet's downstream boundary.

Figure 15(*b*) shows the area of the jet cross-section plotted against the jet length, where a threshold value of scalar concentration is used to differentiate between jet and crossflow fluids. The area is normalized by the jet area at the jet exit (A_0) and, as expected, A_s increases monotonically with s. At a distance of $3d$ from the jet exit, the area of the jet is about ten times that at the jet exit. This ratio increases to about 30 at $s = 6d$ and to about 46 at $s = 9d$. Note that A_s increases sharply between $s = 4d$ and $s = 5d$. Figure 15(*b*) also shows the variation of jet area for a regular turbulent jet, computed in a similar fashion, and using the same threshold value of scalar concentration. The data for this curve corresponds to the simulations presented in Babu & Mahesh (2004, $Re = 2400$). Beginning at about 2 diameters from the jet exit, note that the transverse jet has a significantly larger cross-section than the regular jet. Also, this difference in the area (between the transverse jet and the regular jet) is consistent with their entrainment characteristics (figure 14*a*). Entrainment and jet-area computation are based on a threshold value for the scalar concentration to differentiate between the jet and crossflow fluids. Since the scalar concentration decreases with increasing distance along the jet centreline, the criterion is based on the local scalar maxima. Figures 14 and 15(*b*) show the results when the scalar cutoff is 1% of the local maxima. A change in this cutoff value changes the curves quantitatively, but the trends remain the same. Comparison of these curves at different scalar threshold values is shown in the Appendix.

Entrainment by regular jets is commonly attributed to the coherent motions at the edges of the jet. In the case of transverse jets, the flow field causes more crossflow fluid to come into contact with the jet fluid on the downstream side. This, in turn, results in the downstream side of the jet entraining more fluid than the upstream side, causing much higher entrainment than observed in a regular jet. An explanation of this phenomenon, in terms of the pressure field downstream of the jet, follows.

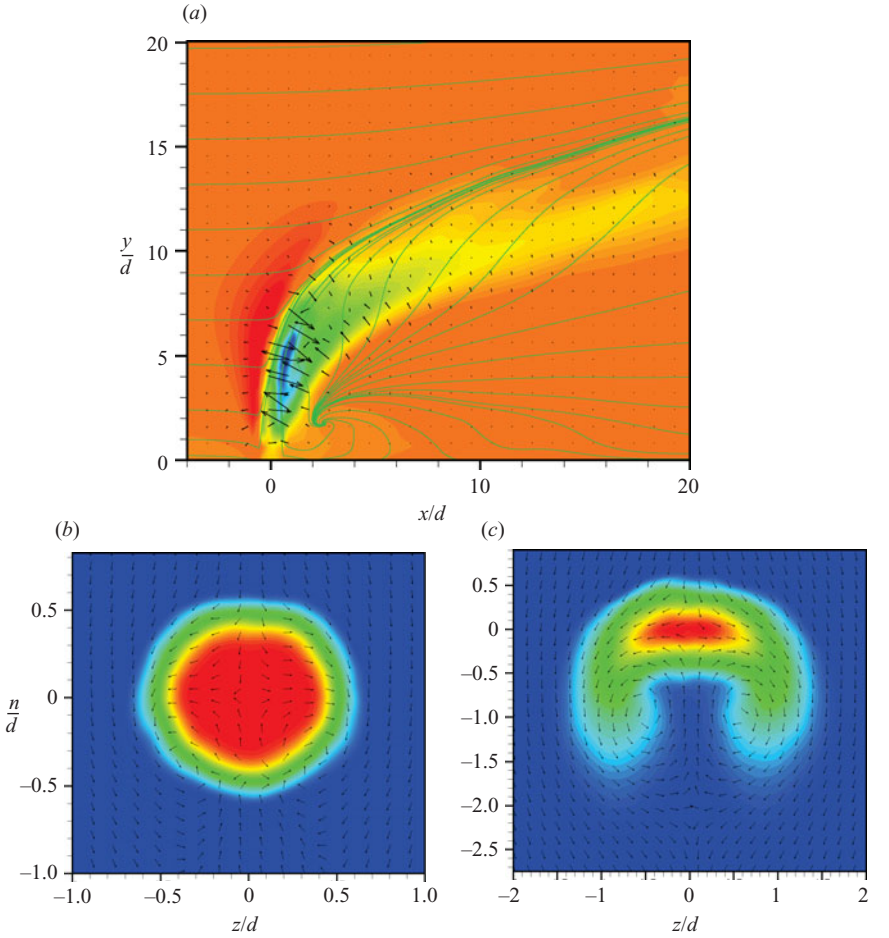

FIGURE 16. (*a*) Contours of pressure on the symmetry plane along with in-plane streamlines (in green). The black vectors indicate the quantity $-\nabla p$ on the symmetry plane. (*b*) Jet cross-section at $s = d$. Contours of scalar along with in-plane velocity vectors. (*c*) Jet cross-section at $s = 4d$, scalar contours, in-plane velocity vectors.

3.4. *Entrainment mechanism*

Figure 16(*a*) shows contours of mean pressure on the symmetry plane. The highest pressure on this plane (shown in red) is observed near the upstream edge of the jet, beginning close to the jet exit/wall and extending until the jet noticeably bends. The lowest pressure (in blue) is observed near the downstream edge of the jet (at about $y \sim 5d$). Moving in the x-direction, the pressure begins to increase past the downstream edge. The vectors in figure 16(*a*) denote the pressure gradient ($-\nabla p$) on the symmetry plane. The direction of the vectors downstream of the jet indicates the tendency of the pressure gradient to drive crossflow fluid toward the jet. The magnitude of these pressure gradients is significant, as evident from the length of the vectors. This pressure field causes large amounts of crossflow fluid to come into contact with the jet fluid, enabling it to be entrained. The presence of the saddle node, acting as a source, in this region of high-pressure gradients further enhances crossflow entrainment on the downstream side.

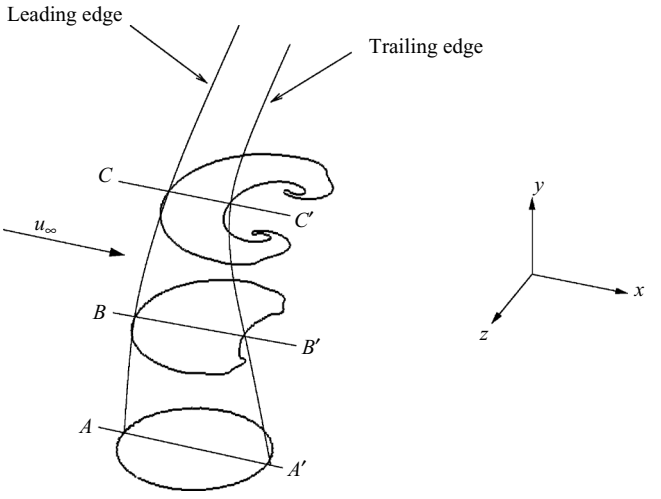

FIGURE 17. Schematic of the near field of the jet.

It is important to differentiate between the $-\nabla p$ vectors near the leading edge of the jet (pointing in the positive-x, positive-y direction), and those downstream of the jet's trailing edge (pointing in the negative-x, positive-y direction). The high-pressure region on the upstream side occurs very close to the jet's leading edge, and follows it. Very few pressure gradient vectors of considerable magnitude originate in the crossflow fluid. Hence, the pressure gradient in this region does not affect the upstream entrainment. On the downstream side, however, the high-pressure region and the resulting pressure gradients are observed at a distance from the jet's trailing edge (as far as about $4d$ away, at $s \sim 6d$) and more than a few vectors of significant magnitude are observed to originate in the downstream crossflow fluid. As a result, the pressure gradient downstream of the jet acts to enhance entrainment, while the upstream pressure gradient bends the jet in the direction of the crossflow, and determines the jet trajectory. Figures 16(b) and 16(c) show the jet cross-section, normal to the trajectory, at $s = d$ and $4d$. Contours of time-averaged scalar concentration are shown, along with in-plane velocity vectors. The jet is barely deformed at $s = d$, and approaches the kidney shape at $s = 4d$. The velocity vectors show the motion of crossflow fluid, downstream of the jet's trailing edge, toward the trailing edge – indicating entrainment on the downstream side.

The pressure gradient on the downstream side may be related to the jet deformation as follows. Figure 17 shows a schematic of the jet in the near-field of the jet exit. The crossflow is in the x-direction and the direction of the jet is along the y-axis. Cross-sections of the jet at three distances from the wall are shown, corresponding to planes A–A', B–B' and C–C'. Section A–A' is very close to the jet exit and section C–C' is the point where the jet begins to bend significantly into the crossflow. At A–A', the jet cross-section is roughly circular, and corresponds to figure 16(b) from the simulation. The jet fluid has a high velocity (as compared to u_∞) and momentum, and the crossflow fluid sees it as an obstacle. Crossflow fluid (on the symmetry plane) decelerates just upstream of the jet, resulting in a high-pressure region as observed in figure 16(a). The figure also shows a high-pressure region just downstream of the trailing edge. The jet fluid has no velocity in the x-direction and is subject to an acceleration in that direction, owing to the crossflow fluid. It can be shown

(Muppidi & Mahesh 2006) that the opposing directions of the pressure gradient and the acceleration on the trailing edge of the jet cause the trailing edge to move closer to the leading edge, deforming the jet from a circular cross-section to a kidney-shaped cross-section. Sections B–B' and C–C' in figure 17 show stages of deformation of the jet cross-section. This change in cross-section is also evident in figure 16(c). As the jet evolves (between A–A' and C–C'), note that the leading edge accelerates, and moves in the direction of the crossflow, while the trailing edge moves closer to the leading edge. This deformation of the jet causes the trailing-edge pressure to decrease, from A' to B' to C'. Crossflow fluid downstream of the trailing edge, however, has a higher pressure and this pressure gradient drives crossflow fluid toward the trailing edge, enhancing entrainment on the downstream side.

As the velocity ratio of the transverse jet increases, it becomes more of a regular jet and its entrainment features (and the jet area) must evolve correspondingly. The present simulation shows that the downstream pressure gradient scales with the crossflow free-stream velocity. However, the location of the minimum pressure appears to depend on the jet trajectory and, hence, on the velocity ratio. As r increases, the jet remains vertical to a greater extent, resulting in a lower (downstream) pressure gradient. The imbalance between downstream and upstream entrainments, seen in figure 14(b), would decrease. As the influence of the pressure gradient decreases, the flow field must show similar entrainment features as seen in the regular jet. It is plausible that an increase in the velocity ratio would increase the distance between the saddle-node and the point on the jet trajectory where the jet fluid changes direction significantly. This would also result in a reduction in the amount of crossflow fluid entrained by the jet.

4. Eddy diffusivity

Most RANS computations of passive scalar mixing use the gradient–diffusion hypothesis. According to this hypothesis (e.g. Pope 2000), the turbulent flux $\langle \boldsymbol{u}'C' \rangle$ is aligned with the mean gradient $-\nabla\langle C \rangle$ of the conserved scalar, i.e. there is a positive constant D_t, turbulent diffusivity (or eddy diffusivity), such that

$$\langle \boldsymbol{u}'C' \rangle = -D_t \nabla \langle C \rangle. \tag{4.1}$$

We use the results of the present DNS to comment upon the applicability of the gradient–diffusion hypothesis for computing scalar transport in transverse jets. Figure 18 shows contours of $\langle u'C' \rangle$ and $\langle v'C' \rangle$ on the symmetry plane (in greyscale contours) along with (line) contours of $\partial\langle C \rangle/\partial x$ and $\partial\langle C \rangle/\partial y$, respectively. As predicted by the gradient–diffusion hypothesis, figure 18 shows that regions of the mean scalar gradient appear visually to coincide with regions of turbulent scalar flux. Equation (4.1) can be written for the different components as

$$\langle u'C' \rangle = -D_{t1}\frac{\partial\langle C \rangle}{\partial x}, \langle v'C' \rangle = -D_{t2}\frac{\partial\langle C \rangle}{\partial y}, \langle w'C' \rangle = -D_{t3}\frac{\partial\langle C \rangle}{\partial z}. \tag{4.2}$$

The gradient–diffusion hypothesis (equation (4.1)) assumes isotropic behaviour, which requires that the constants in (4.2) follow $D_{t1} = D_{t2} = D_{t3}$.

The results of the present simulation are used to examine (i) equation (4.2) (does the scalar flux vary linearly with the mean scalar gradient?), and (ii) the isotropy assumption (is $D_{t1} = D_{t2} = D_{t3}$?). Figure 19(a) shows the variation of the streamwise scalar flux $\langle u'C' \rangle$ with the mean scalar gradient $\partial\langle C \rangle/\partial x$ on the symmetry plane. The symbols correspond to every computational point in the window $-2 \leqslant x/d \leqslant 4$ and

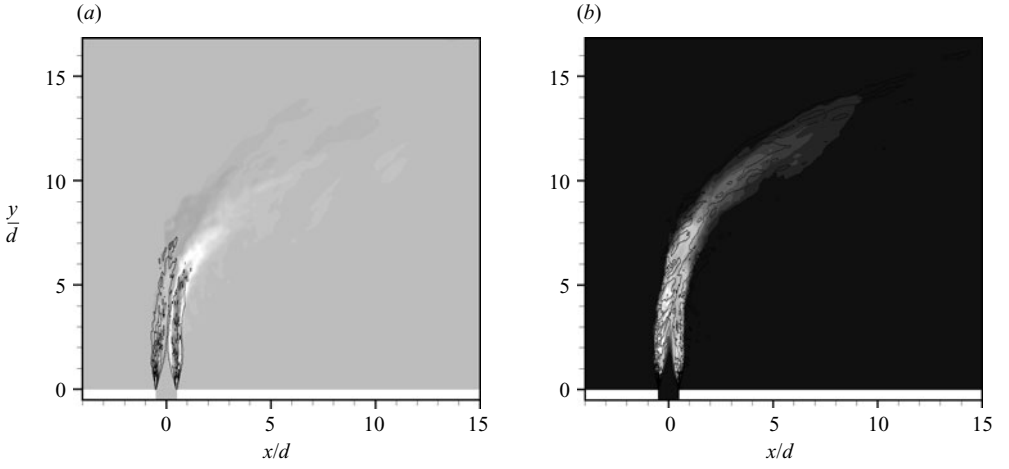

FIGURE 18. Contours of scalar flux (flood) and mean scalar gradient (lines) on the symmetry plane. (*a*) $\overline{u'C'}$ and $\partial\overline{C}/\partial x$, (*b*) $\overline{v'C'}$ and $\partial\overline{C}/\partial y$.

	Direction	D_{ti}
Molecular diffusivity $D = 1.34 \times 10^{-4}$	x	$D_{t1} = 0.08141$
	y	$D_{t2} = 0.38679$
	z	$D_{t3} = 0.00761$
	All	$D_t = 0.02987$

TABLE 1. The different diffusivities computed using symmetry plane scalar field.

$0 \leqslant y/d \leqslant 10$. From figure 18, this region appears to be where the gradient–diffusion hypothesis is most applicable. The thin straight line in the figure is a least-squares fit for a linear variation. It is encouraging that a significant bulk of the data lies close to this line. The value of D_{t1} corresponding to its slope is presented in table 1.

Similar plots for D_{t2} and D_{t3} are shown in figures 19(*b*) and 19(*c*), respectively. In both cases, the scatter appears greater than that seen in figure 19(*a*). Also, peak values (both negative and positive) of $\partial\langle C\rangle/\partial y$ and $\partial\langle C\rangle/\partial z$ are much smaller than the peak (negative and positive) $\partial\langle C\rangle/\partial x$. Once again, the lines indicate the best linear fit for the variables and the values of D_{t2} and D_{t3} are shown in table 1. Note the difference in the three diffusivity values.

A single value of scalar diffusivity may be computed by equating the measured and modelled production of the passive scalar variance, as given by

$$P_{ii} = -\overline{C'u_i'}\frac{\partial\overline{C}}{\partial x_i} = D_t\frac{\partial\overline{C}}{\partial x_i}\frac{\partial\overline{C}}{\partial x_i}, \tag{4.3}$$

which may be re-written as

$$D_t = \frac{P_{ii}}{\dfrac{\partial\overline{C}}{\partial x_i}\dfrac{\partial\overline{C}}{\partial x_i}}. \tag{4.4}$$

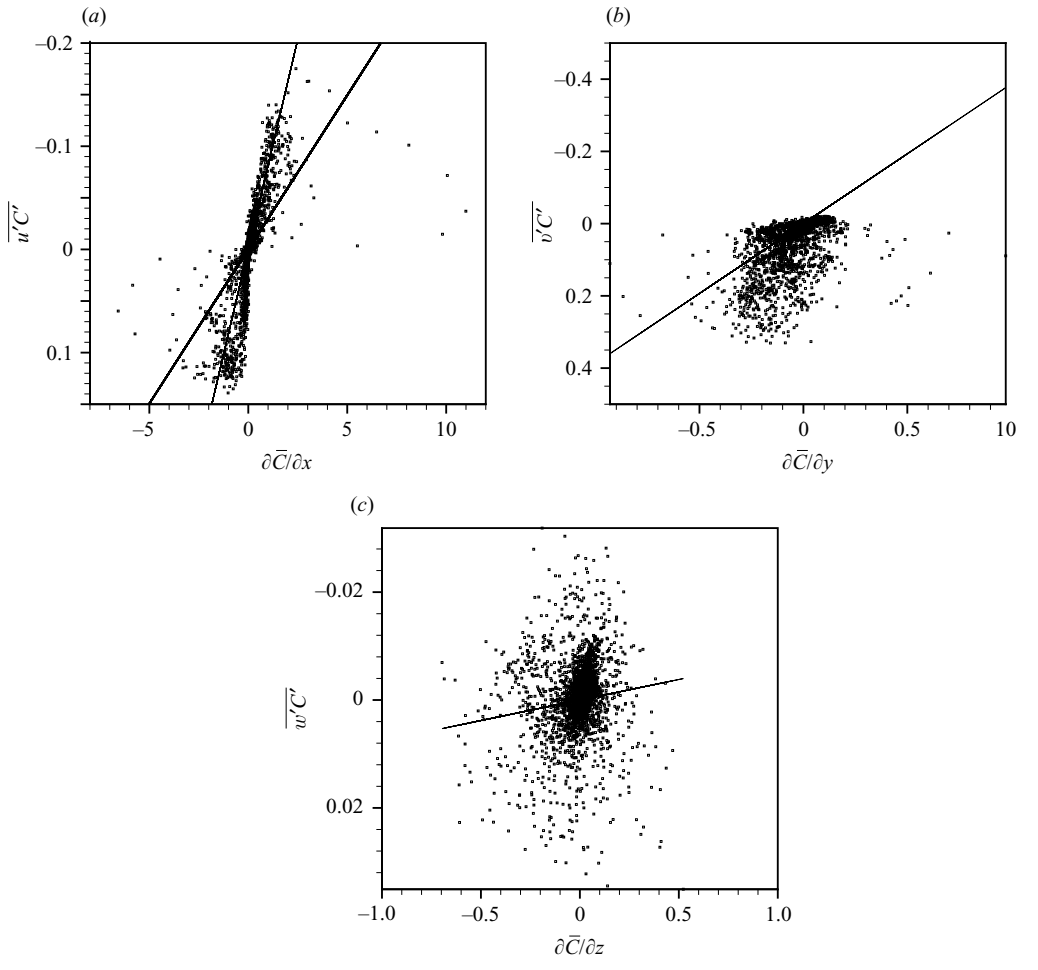

FIGURE 19. Variation of the scalar flux with the mean scalar gradient. (*a*) $\overline{u'C'}$ *vs.* $\partial\overline{C}/\partial x$, (*b*) $\overline{v'C'}$ *vs.* $\partial\overline{C}/\partial y$, and (*c*) $\overline{w'C'}$ *vs.* $\partial\overline{C}/\partial z$. The thin lines show least-squares fit for D_{t1}, D_{t2} and D_{t3}, respectively. The thick line in (*a*) shows the overall diffusivity D_t.

Equation (4.4) is equivalent to obtaining D_t as a least-squares fit to the three diffusivities D_{t1}, D_{t2} and D_{t3}. Table 1 also gives the value for D_t, which is significantly different from each of D_{t1}, D_{t2} and D_{t3}. The overall diffusivity is also indicated by the thick line in figure 19(*a*). Note that D_t is poor at describing the relation between $\langle u'C'\rangle$ and $\partial\langle C\rangle/\partial x$.

4.1. *Counter-gradient diffusion*

The gradient–diffusion hypothesis assumes that the turbulent diffusivity D_t is a positive scalar. This implies that the scalar flux is in the same direction as the mean scalar gradient, i.e. the transport of scalar (by this term) is always in the direction from a region of higher mean scalar concentration to a lower one. In figure 19(*a*), all of the points lie in two quadrants indicating that while there is a scatter in the value of D_{t1}, the diffusivity is positive at all the elements. However, this is not the case with figures 19(*b*) and 19(*c*). A large number of points lie in the quadrants implying a non-positive turbulent diffusivity, i.e. counter gradient diffusion. The present results

show that almost all of the points in figure 19(*b*) with negative D_{t2} values correspond to the leading and the trailing edges of the jet. Elements close to the boundary layer ($-2 \leqslant x/d \leqslant -0.5$, $0 \leqslant y/d \leqslant 0.5$) also show a negative D_{t2}, but correspond to very low ($O[10^{-10}]$) values of the scalar gradient and can be neglected. Hence, it may be concluded that the leading and trailing edges of the jet exhibit counter gradient diffusion while the rest of the symmetry plane exhibits gradient diffusion.

Counter-gradient diffusion is often observed in combustion problems (Bray *et al.* 1981; Libby & Bray 1981; Veynante *et al.* 1997). The prevalent understanding is that gradient diffusion occurs when the flow field is dominated by turbulent motions, and that counter-gradient diffusion occurs when the flow field is dominated by thermal dilatation as a result of chemical reactions. However, the present problem exhibits counter-gradient diffusion in the absence of any chemical reactions. In a turbulent channel flow, no negative (eddy) diffusivity is observed. However, Seki & Kawamura (2004) report the existence of a counter-gradient diffusion region in a turbulent channel flow when asymmetric boundary conditions are prescribed for the scalar. Counter-gradient transfer has also been observed in asymmetric wakes (Sreenivasan, Tavoularis & Corrsin 1982). Both examples suggest that asymmetric scalar boundary conditions can cause counter-gradient diffusion in the absence of chemical reactions. Tagawa, Matsubara & Ohta (2002) consider a turbulent non-premixed flame formed in a curved rectangular duct, which exhibits counter-gradient diffusion. As the flow turns, pressure increases from the inner wall toward the outer wall, and their results show that the onset of counter-gradient diffusion is related to this radial pressure gradient. They observe gradient diffusion in the vicinity of the inner wall and counter-gradient diffusion toward the outer wall. They explain this feature as a result of the 'damping' of the fluid motion owing to the high-pressure region near the outer wall of the duct. The transverse jet is subject to significant pressure gradients in the vicinity of its leading and trailing edges, that accelerate the jet fluid, and determine the jet trajectory. This near-field pressure gradient, and the resulting asymmetry of the flow field (about the $x = 0$ plane) probably cause the observed counter-gradient diffusion of the passive scalar.

5. Summary

Direct numerical simulation of passive scalar transport in a turbulent transverse jet is performed. The conditions of the simulation correspond to an experiment by Su & Mungal (2004). Quantitatively, mean scalar profiles show a very good agreement between the simulation and the experiment while comparison of scalar variance shows a difference. The peak $\langle C'C' \rangle$ from the simulation is higher than that from the experiment at all the locations. Increased mixing in the near field of a jet in crossflow can be related to its enhanced entrainment as compared to that of a regular jet. It is observed that entrainment is significantly higher on the downstream side of the jet than on the upstream side. The crossflow fluid exerts a pressure gradient along the leading edge, accelerating the jet in the streamwise direction. The pressure gradient near the trailing edge of the jet exit opposes this acceleration. As a result, the jet cross-section deforms, and the trailing-edge pressure decreases along the jet length. The resulting pressure field, along with the three-dimensionality of the flow field, drives downstream crossflow fluid toward the jet, causing the increased entrainment as observed. The results of the simulation are used to test the gradient–diffusion hypothesis for passive scalar transport. Variation of the turbulent flux with the mean scalar gradient is not as linear as would be desired, and the assumption of isotropy is

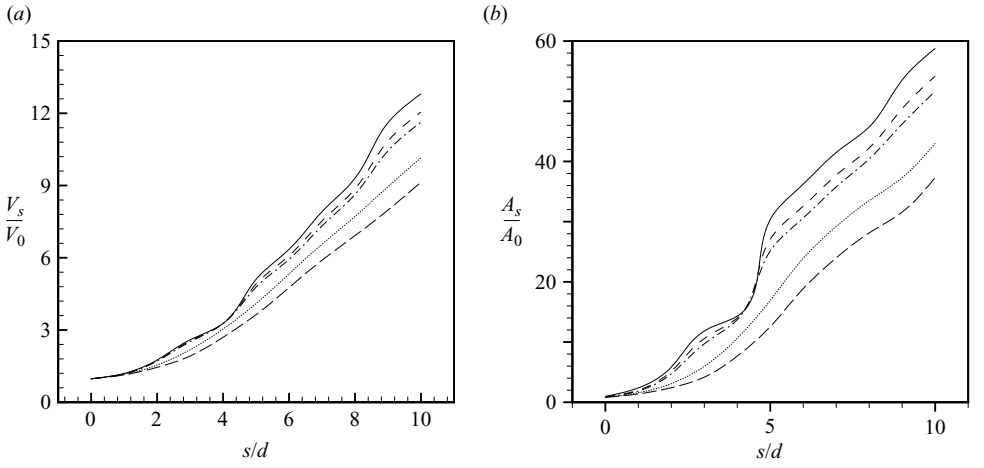

FIGURE 20. (*a*) Entrainment plotted as a function of s for various values of the scalar threshold C_c. (*b*) Jet area versus s for different C_c. ———, $C_c/C_{max} = 0.001$; – – –, $C_c/C_{max} = 0.005$; — · —, $C_c/C_{max} = 0.01$; . . . , $C_c/C_{max} = 0.05$; — — —, $C_c/C_{max} = 0.1$.

invalid. The strong pressure gradients in the near field also cause the flow to exhibit regions of counter-gradient diffusion.

Appendix. Sensitivity of entrainment to scalar cutoff

In order to compute both the jet area and the entrainment in this flow, a threshold value for the scalar concentration (C_c) was used to differentiate between the scalar-carrying jet fluid and the crossflow fluid. C_c can be specified based on either the maximum scalar concentration C_0, or the local maxima C_{max}. Along the jet length, the scalar concentration decreases significantly, as observed in figures 7(*a*) and 7(*b*). Hence, C_c is defined as a fraction of C_{max} for the results presented in this paper.

The entrainment and jet area are sensitive to C_c, as figure 20 shows. The effect of different C_c/C_{max} on the jet volume flux is shown in figure 20(*a*), while that on the computation of the jet area is shown in figure 20(*b*). The different thresholds considered are $C_c/C_{max} = 0.001$, 0.005, 0.01, 0.05 and 0.1. At any s, a decrease in C_c/C_{max} increases the volume of the scalar-carrying fluid and, hence, the jet area and the volume flux. While the curves do not quite show any convergence during this range of $C_c/C_{max} \in [0.001,0.1]$, the difference does appear to decrease with decreasing C_c/C_{max}. While the curves are quantitatively dependent on the scalar cutoff, the behaviour of the curves appears the same at all values of C_c. Further, it appears that the choice of $C_c/C_{max} = 0.01$ results in a fair description of the entrainment (and jet area) characteristics. The results presented in § 3.3 are based on this cutoff value for the scalar.

This work was supported by the National Science Foundation under grant CTS–0133837. Computer time was provided by The National Center for Supercomputing Applications (NCSA), Minnesota Supercomputing Institute (MSI) and the San Diego Supercomputer Center (SDSC). We thank Professors Su and Mungal for making their data available, and for several useful discussions.

REFERENCES

Acharya, S., Tyagi, M. & Hoda, A. 2001 Flow and heat transfer predictions for film-cooling. *Ann. NY Acad. Sci.* **934**, 110–125.

Andreopoulos, J. & Rodi, W. 1984 Experimental investigation of jets in a crossflow. *J. Fluid Mech.* **138**, 93–127.

Babu, P. & Mahesh, K. 2004 Upstream entrainment in numerical simulation of spatially evolving round jets. *Phys. Fluids* **16**, 3699–3705.

Bray, K. N. C., Libby, P. A., Masuya, G. & Moss, J. B. 1981 Turbulence production in premixed turbulent flames. *Combust. Sci. Technol.* **25**, 127–140.

Broadwell, J. E. & Breidenthal, R. E. 1984 Structure and mixing of a transverse jet in incompressible flow. *J. Fluid Mech.* **148**, 405–412.

Chochua, G., Shyy, W., Thakur, S., Brankovic, A., Lienau, K., Porter, L. & Lischinsky, D. 2000 A computational and experimental investigation of turbulent jet and crossflow interaction. *Numer. Heat Transfer* A **38**, 557–572.

Dowling, D. R. & Dimotakis, P. E. 1990 Similarity of the concentration field of gas-phase turbulent jets. *J. Fluid Mech.* **218**, 109–141.

Eggels, J. G. M., Unger, F., Weiss, M. H., Westerweel, J., Adrian, R. J., Friedrich, R. & Nieuwstadt, T. M. 1994 Fully developed turbulent pipe flow: a comparison between numerical simulation and experiment. *J. Fluid Mech.* **268**, 175–209.

Fearn, R. L. & Weston, R. P. 1974 Vorticity associated with a jet in crossflow. *AIAA J.* **12**, 1666–1671.

Fric, T. F. & Roshko, A. 1994 Vortical structure in the wake of a transverse jet. *J. Fluid Mech.* **279**, 1–47.

Hasselbrink, E. F. & Mungal, M. G. 2001 Transverse jets and jet flames. Part 1. Scaling laws for strong transverse jets. *J. Fluid Mech.* **443**, 1–25.

Herrmann, M., Blanquart, G. & Raman, V. 2004 Flux corrected finite-volume scheme for preserving scalar boundedness in large-eddy simulations. In *Annu. Res. Briefs 2004*, pp. 75–85. Center for Turbulence Research, Stanford, CA.

Karagozian, A. R. 1986 An analytical model for the vorticity associated with a transverse jet. *AIAA J.* **24**, 429–436.

Kamotani, Y. & Greber, I. 1972 Experiments on turbulent jet in a crossflow. *AIAA J.* **10**, 1425–1429.

Kelso, R. M., Lim, T. T. & Perry, A. E. 1996 An experimental study of round jets in cross-flow. *J. Fluid Mech.* **306**, 111–144.

Krothapalli, A., Lourenco, L. & Buchlin, J. M. 1990 Separated flow upstream of a jet in a crossflow. *AIAA J.* **28**, 414–420.

Libby, P. A. & Bray, K. N. C. 1981 Countergradient diffusion in premixed turbulent flames. *AIAA J.* **19**, 205–213.

Mahesh, K., Constantinescu, G. & Moin, P. 2004 A numerical method for large-eddy simulation in complex geometries. *J. Comput. Phys.* **197**, 215–240.

Margason, R. J. 1993 Fifty years of jet in crossflow research. In *AGARD Symp. on a Jet in Cross Flow, Winchester, UK. AGARD CP* 534.

Muppidi, S. & Mahesh, K. 2005 Study of trajectories of jets in crossflow using direct numerical simulations. *J. Fluid. Mech.* **530**, 81–100.

Muppidi, S. & Mahesh, K. 2006 A two-dimensional model problem to explain CVP formation in a transverse jet. *Phys. Fluids* **18**, 085103.

Muppidi, S. & Mahesh, K. 2007 Direct numerical simulation of round turbulent jets in crossflow. *J. Fluid. Mech.* **574**, 59–84.

Pope, S. B. 2000 *Turbulent Flows*. Cambridge University Press.

Ricou, F. P. & Spalding, D. B. 1961 Measurements of entrainment by axisymmetrical turbulent jets. *J. Fluid. Mech.* **11**, 21–32.

Schlichting, H. T. 1968 *Boundary Layer Theory*. McGraw-Hill.

Schluter, J. U. & Schonfeld, T. 2000 LES of jets in crossflow and its application to a gas turbine burner. *Flow Turbulence Combust.* **65**, 177–203.

Seki, Y. & Kawamura, H. 2004 DNS of turbulent heat transfer in a channel flow with a streamwisely varying thermal boundary condition. *15th Australasian Fluid Mech. Conf. The University of Sydney, Sydney, Australia.*

Shan, J. W. & Dimotakis, P. E. 2006 Reynolds-number effects and anisotropy in transverse-jet mixing. *J. Fluid. Mech.* **566**, 47–96.

Smith, S. H. & Mungal, M. G. 1998 Mixing, structure and scaling of the jet in crossflow. *J. Fluid Mech.* **357**, 83–122.

Sreenivasan, K. R., Tavoularis, S. & Corrsin, S. 1982 *A Test of Gradient Transport and its Generalizations. Turbulent Shear Flows*, vol. 3, pp. 96–112. Springer.

Su, L. K. & Mungal, M. G. 2004 Simultaneous measurement of scalar and velocity field evolution in turbulent crossflowing jets *J. Fluid Mech.* **513**, 1–45.

Tagawa, M., Matsubara, F. & Ohta, Y. 2002 *Combust. Flame* **129**, 151–163.

Veynante, D., Trouve, A., Bray, K. N. C. & Mantel, T. 1997 Gradient and counter-gradient scalar transport in turbulent premixed flames. *J. Fluid Mech.* **332**, 263–293.

Yuan, L. L. & Street, R. L. 1998 Trajectory and entrainment of a round jet in crossflow. *Phys. Fluids* **10**, 2323–2335.

Yuan, L. L., Street, R. L. & Ferziger, J. H. 1999 Large-eddy simulations of a round jet in crossflow. *J. Fluid Mech.* **379**, 71–104.